AIAA JOURNAL
Vol. 43, No. 2, February 2005

Evaluation of High-Order Spectral Volume Method for Benchmark Computational Aeroacoustic Problems

Z. J. Wang*
Michigan State University, East Lansing, Michigan 48824

A time-accurate, high-order finite volume method named spectral volume (SV) method has been developed recently for conservation laws on unstructured grids and successfully demonstrated for Euler equations. In this paper, the SV method is evaluated for several benchmark problems in computational aeroacoustics (CAA) to demonstrate its potential for CAA applications. Both one-dimensional and two-dimensional problems are tested in the evaluation. It is shown that the higher-order SV schemes can achieve the same accuracy at a much lower cost than the lower-order ones.

Nomenclature

A = nozzle cross-section area
B = flux Jacobian matrix
$C_{i,j}$ = jth control volume of the ih spectral volume
c = sound speed
E = inviscid flux vector in x direction
E_t = total energy
F = inviscid flux vector in y direction
$\boldsymbol{f}$ = (E) in one dimension or (E, F) in two dimensions
$\hat{f}$ = numerical (Riemann) flux
h = mesh size
k = degree of polynomials
L = shape function
M = Mach number
m = dimension of the space of polynomials
N = number of cells
$\boldsymbol{n}$ = unit surface normal
P = space of polynomials
p = pressure
Q = vector of conserved variables
R = matrix composed of right eigenvectors of B
$\boldsymbol{r}$ = position vector
S = source vector
S_i = spectral volume i
u = velocity in x direction
V = volume
v = velocity in y direction
γ = ratio of specific heats
Λ = diagonal matrix composed of the eigenvalues of B
λ = eigenvalues of B
ρ = density
Ω = computational domain
ω = angular frequency

I. Introduction

A NEW high-order finite volume (FV) method named the spectral volume (SV) method has been developed recently for hyperbolic conservations laws and successfully demonstrated for both scalar and system conservation laws.[1–4] The SV method is a Godunov-type finite volume method,[5,6] which has been under development for over three decades, and has become the state of the art for the numerical solution of hyperbolic conservation laws. The SV method is also related to the discontinuous Galerkin (DG) method,[7,8] multidomain spectral method,[9] and unstructured spectral method,[10] which have been applied to the computation of wave propagation successfully. Comparisons between the DG and SV methods have been made recently.[11,12] The SV method avoids the volume integral required in the DG method. However, it does introduce more interfaces where more Riemann problems are solved. For two-dimensional Euler equations, both methods seem to achieve similar efficiency.[11] Both the DG and SV methods are capable of achieving the optimal order of accuracy. The DG method usually has a lower error magnitude, but the SV method allows larger time steps. Because of its inherent property of subcell resolution, the SV method is capable of capturing discontinuities with a higher resolution than the DG method. For a review of the literature on the Godunov-type FV and DG methods, refer to Ref. 1 and the references therein. Like all Godunov-type finite volume methods, the SV method has two key components: one is data reconstruction, and the other is the (approximate) Riemann solver. What distinguishes the SV method from the k-exact finite volume method[13] is in the data reconstruction. Instead of using a (large) stencil of neighboring cells to perform a high-order polynomial reconstruction, the unstructured grid cell—called a spectral volume—is partitioned into a "structured" set of subcells called control volumes (CV), and cell averages on these subcells are then the degrees of freedom (DOFs). These DOFs are used to reconstruct a high-order polynomial inside the macro-element, that is, the SV. If all of the spectral volumes are partitioned in a geometrically similar manner, the expression for the reconstruction in terms of the DOFs is universal for any simplex regardless of their shapes. This is because all simplex can be mapped into a standard simplex using a linear transformation. After the reconstruction step, the DOFs are updated to high-order accuracy using the usual finite volume method. Numerical tests with conservation laws in both one and two dimensions have verified that the SV method is indeed highly accurate, conservative, and geometrically flexible.[1–4]

In this paper, the SV method is evaluated for several benchmark problems in computational aeroacoustics (CAA). As pointed out by Tam,[14] acoustic waves have their own characteristics that make their computation unique and challenging. Acoustic waves are inherently unsteady. Their amplitudes are several orders smaller than the magnitudes of the mean flow, and their frequencies are generally very high and broad ranging. Computational methods with high-order accuracy are required to capture the acoustic portion of the solution.[15–17] Over the last decade, many high-order algorithms such as compact schemes,[15,17] dispersion-relation-preserving schemes[16] have been developed and applied successfully in many

Presented as Paper 2003-0880 at the 41st Aerospace Sciences Meeting, Reno, NV, 6–9 January 2003; received 23 March 2004; revision received 11 August 2004; accepted for publication 13 August 2004.

*Associate Professor, Department of Mechanical Engineering; currently Associate Professor of Aerospace Engineering, 2271 Howe Hall, Room 1200, Iowa State University, Ames, IA 50011-2271; zjw@egr.msu.edu. Associate Fellow AIAA.

CAA applications. These schemes were developed for Cartesian grid or smooth structured grids, and therefore the applications of these methods are limited to relatively simple geometries. For problems with complex geometries, it is a considerable challenge to generate any structured grid, let alone a smooth structured grid, which can preserve the high-order accuracy of the numerical algorithms. We, therefore, advocate an unstructured grid approach for complex configurations. The requirement of geometric flexibility comes from the desire to compute noise over real-world configurations, such as aircraft or car geometries. Unfortunately, the majority of existing numerical algorithms for unstructured grids are at best second-order accurate and not accurate enough to capture the acoustic portion in the flowfield. In this study, the SV method is put to the test for CAA benchmark problems.

The paper is organized as follows. In the next section, the basic formulation of the SV method for the Euler equations is reviewed. In Sec. III, several CAA benchmark cases, both one- and two-dimensional problems, are presented. Finally, conclusions and recommendations for further investigations are summarized in Sec. IV.

II. Spectral (Finite) Volume Method for Euler Equations

A. Governing Equations

Although aeroacoustic waves are governed by the Navier–Stokes equations, in the present study the nonlinear Euler equations are considered for wave propagation using benchmark problems. One of the motivations of employing the nonlinear equations is to tackle problems of shock/acoustic-wave interactions. The unsteady two-dimensional Euler equation in conservation form can be written as

$$\frac{\partial Q}{\partial t}+\frac{\partial E}{\partial x}+\frac{\partial F}{\partial y}=0 \tag{1a}$$

$$Q=\begin{Bmatrix}\rho\\ \rho u\\ \rho v\\ E_t\end{Bmatrix},\qquad E=\begin{Bmatrix}\rho u\\ \rho u^2+p\\ \rho uv\\ u(E_t+p)\end{Bmatrix},\qquad F=\begin{Bmatrix}\rho v\\ \rho uv\\ \rho v^2+p\\ v(E_t+p)\end{Bmatrix} \tag{1b}$$

The pressure is related to the total energy by

$$E_t=p/(\gamma-1)+\tfrac{1}{2}\rho(u^2+v^2) \tag{1c}$$

with a constant ratio of specific heats γ. The Euler equations (1) are hyperbolic because the Jacobian matrix of the flux vector in direction $\boldsymbol{n}=(n_x, n_y)$

$$B=n_x\frac{\partial E}{\partial Q}+n_y\frac{\partial F}{\partial Q} \tag{2}$$

has all real eigenvalues and a complete set of eigenvectors. In fact, B has four real eigenvalues $\lambda_{1,2}=v_n$, $\lambda_3=v_n+c$, $\lambda_4=v_n-c$, and a complete set of (right column) eigenvectors $\{r_1, r_2, r_3, r_4\}$, where $v_n=un_x+vn_y$. Let R be the matrix composed of these right eigenvectors, then the Jacobian matrix B can be diagonalized as

$$R^{-1}BR=\Lambda \tag{3}$$

where Λ is the diagonal matrix containing the eigenvalues, that is, $\Lambda=diag(v_n, v_n, v_n+c, v_n-c)$.

The degeneration of the two-dimensional Euler equations into the one-dimensional equations is obvious. However, if one considers one-dimensional flows in ducts with an area variation, the following equations are obtained:

$$\frac{\partial Q}{\partial t}+\frac{\partial E}{\partial x}=S \tag{4a}$$

where

$$Q=\begin{Bmatrix}\rho\\ \rho u\\ E_t\end{Bmatrix},\qquad E=\begin{Bmatrix}\rho u\\ \rho u^2+p\\ u(E_t+p)\end{Bmatrix}$$

$$S=\begin{Bmatrix}-\rho u\dfrac{1}{A}\dfrac{\partial A}{\partial x}\\ -\rho u^2\dfrac{1}{A}\dfrac{\partial A}{\partial x}\\ -\dfrac{u(E_t+p)}{A}\dfrac{\partial A}{\partial x}\end{Bmatrix} \tag{4b}$$

In the following presentation, both the one- and two-dimensional numerical algorithms are treated in the same manner. We therefore recast the governing equations uniformly as

$$\frac{\partial Q}{\partial t}+\nabla\cdot\boldsymbol{f}=S \tag{5}$$

where $\boldsymbol{f}=(E)$ in one dimensions and $\boldsymbol{f}=(E, F)$ in two dimensions.

B. Spectral Volume Method for the Euler Equations

Assume that the Euler equations (5) are solved in the computational domain Ω subject to proper initial and boundary conditions. The domain is discretized into N nonoverlapping simplex elements (i.e., line segments in one dimension, and triangular elements in two dimensions) called spectral volumes:

$$\Omega=\bigcup_{i=1}^{N}S_i \tag{6}$$

To support a degree k polynomial reconstruction within each SV, the SV is further partitioned into m subcells, with m given by

$$m=\begin{cases}k+1, & 1D\\ (k+1)(k+2)/2, & 2D\end{cases} \tag{7}$$

Note that m is also the dimension of P^k, the space of polynomials of degree at most k. It has been found in earlier studies[1,2] that the proper partitioning of a SV into CVs is critical to the accuracy and stability of the method. In one-dimension, the partition using the Gauss–Lobatto points defined over $[-1, 1]$, that is,

$$x_{i,j+\frac{1}{2}}=-\cos(j\pi/m),\qquad j=0,\ldots,m \tag{8}$$

gives accurate and convergent results. In two dimensions, many candidate partitions are evaluated.[4] It was found that the partitions for various k shown in Fig. 1 perform satisfactorily. Denote the jth CV of S_i by $C_{i,j}$.The cell-averaged conservative variable Q at time t in control volume $C_{i,j}$ is defined as

$$\bar{Q}_{i,j}(t)=\int_{C_{i,j}}Q(\boldsymbol{r},t)\,\mathrm{d}V\Big/V_{i,j} \tag{9}$$

where $V_{i,j}$ is the volume of $C_{i,j}$. In the SV method, the DOFs or unknowns are the cell-averaged conservative variable Q at the subcells or the CVs. Given the DOFs $\{\bar{Q}_{i,j}\}$, a polynomial $p_i\in P^k$ can be reconstructed such that it is a $(k+1)$th-order accurate approximation to the solution Q inside S_i:

$$p_i(\boldsymbol{r})=Q(\boldsymbol{r})+O(h^{k+1}),\qquad \boldsymbol{r}\in S_i \tag{10}$$

where h is the maximum edge length. This reconstruction can be solved analytically by satisfying the following conditions:

$$\int_{C_{i,j}}p_i(\boldsymbol{r})\,\mathrm{d}V\Big/V_{i,j}=\bar{Q}_{i,j},\qquad j=1,\ldots,m \tag{11}$$

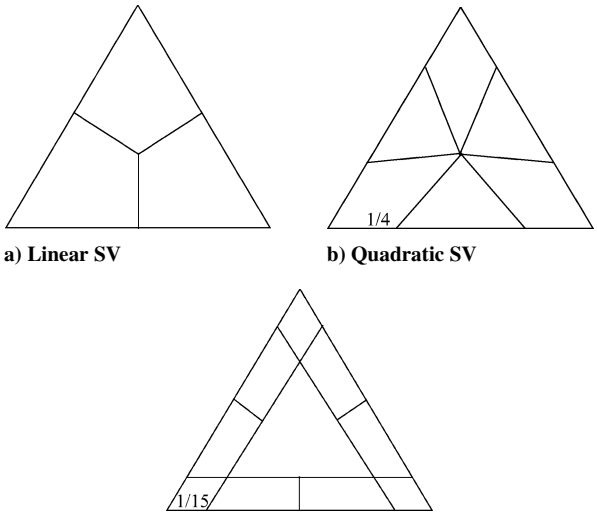

a) Linear SV **b) Quadratic SV**

c) Cubic SV

Fig. 1 Spectral volumes of various degrees.

The reconstruction can be more conveniently expressed as

$$p_i(\boldsymbol{r}) = \sum_{j=1}^{m} L_j(\boldsymbol{r})\,\bar{Q}_{i,j} \tag{12}$$

where $L_j(\boldsymbol{r}) \in P^k$ are the shape functions, which satisfy

$$\int_{C_{i,j}} L_m(\boldsymbol{r})\,\mathrm{d}V \Big/ V_{i,j} = \delta_{\mathrm{jm}} \tag{13}$$

The shape functions can be computed analytically using commercial software capable of performing symbolic manipulations. The shape function formulas are given in Refs. 1 and 4 for one- and two-dimensions reconstructions. The high-order reconstruction is then used to generate high-order updates for the DOFs using the usual FV method. Integrating Eq. (5) in $C_{i,j}$, we obtain the following integral equation for the DOFs:

$$\frac{\mathrm{d}\bar{Q}_{i,j}}{\mathrm{d}t} + \frac{1}{V_{i,j}} \sum_{r=1}^{K} \int_{A_r} (\boldsymbol{f}\cdot\boldsymbol{n})\,\mathrm{d}A = \frac{1}{V_{i,j}} \int_{C_{i,j}} S\,\mathrm{d}V \tag{14}$$

where K is the number of faces in $C_{i,j}$, and A_r represents the rth face of $C_{i,j}$. The surface and volume integrals on each face are performed with Gauss quadrature formulas, which are exact for degree k polynomials, that is,

$$\int_{A_r} (\boldsymbol{f}\cdot\boldsymbol{n})\,\mathrm{d}A \approx \sum_{q=1}^{J} w_{\mathrm{rq}}\,\boldsymbol{f}\,[Q(\boldsymbol{r}_{\mathrm{rq}})]\cdot n_r A_r \tag{15}$$

$$\int_{C_{i,j}} S\,\mathrm{d}A \approx \sum_{q=1}^{M} w_q S(\boldsymbol{r}_q) V_{i,j} \tag{16}$$

where J and M are the number of quadrature points for surface and volume integrals respectively, w_{rq} and w_q are the Gauss quadrature weights, and $\boldsymbol{r}_{\mathrm{rq}}$ and $\boldsymbol{r}_q$ are the Gauss quadrature points. With the SV-wise polynomial reconstructions, no continuity is required at the interfaces of the SVs. Therefore, the state variables are discontinuous across the SV boundaries. The flux vectors at the quadrature points $\boldsymbol{f}[Q(\boldsymbol{r}_{\mathrm{rq}})]$ are not uniquely defined because two different solutions exist on the left- and right-hand sides of the interface. The saving grace for this difficulty is the well-known approximate Riemann solvers[14,15] used in the Godunov-type finite volume method, that is,

$$\boldsymbol{f}[Q(\boldsymbol{r}_{\mathrm{rq}})]\cdot\boldsymbol{n}_r \approx \hat{f}[Q_L(\boldsymbol{r}_{\mathrm{rq}}),\, Q_R(\boldsymbol{r}_{\mathrm{rq}}),\, \boldsymbol{n}_r] \tag{17}$$

where Q_L and Q_R are the vector of conserved variables just to the left and right of the interface. It is the Riemann solver that introduces the upwinding and dissipation into the SV method such that the SV method is not only high-order accurate, but also stable. In this paper, we employ and test two approximate Riemann solvers, that is, Rusanov[18] and Roe[19] fluxes.

The Rusanov flux can be expressed as

$$\hat{f}(Q_L,\, Q_R,\, \boldsymbol{n}) = \tfrac{1}{2}[f_n(Q_L) + f_n(Q_R) - (|\bar{v}_n| + \bar{c})(Q_R - Q_L)] \tag{18}$$

where $f_n = \boldsymbol{f}\cdot\boldsymbol{n}$ and $\bar{v}_n$ and $\bar{c}$ are the average normal velocity and speed of sound at the face.

The Roe flux can be computed from

$$\hat{f}(Q_L,\, Q_R,\, \boldsymbol{n}) = \tfrac{1}{2}[f_n(Q_L) + f_n(Q_R) - |\bar{B}|(Q_R - Q_L)] \tag{19}$$

where $|\bar{B}|$ is the dissipation matrix given by

$$|\bar{B}| = R|\bar{\Lambda}|R^{-1} \tag{20}$$

Here $|\bar{\Lambda}|$ is the diagonal matrix composed of the absolute values of the eigenvalues of the Jacobian matrix evaluated at the so-called Roe-averages.[19] No entropy fixes were employed in all of the simulations.

Finally substituting Eqs. (15–17) into Eq. (14), we obtain the following semidiscrete SV scheme:

$$\frac{\mathrm{d}\bar{Q}_{i,j}}{\mathrm{d}t} + \frac{1}{V_{i,j}} \sum_{r=1}^{K} \sum_{q=1}^{J} w_{\mathrm{rq}}\,\hat{f}[Q_L(\boldsymbol{r}_{\mathrm{rq}}),\, Q_R(\boldsymbol{r}_{\mathrm{rq}}),\, \boldsymbol{n}_r]A_r = \sum_{q=1}^{M} w_q S(\boldsymbol{r}_q) \tag{21}$$

C. Time Integration

For time integration, we use the third-order total-variation-diminishing (TVD) Runge–Kutta scheme.[20] We first rewrite Eq. (21) in a concise ordinary differential equation form

$$\frac{\mathrm{d}\bar{Q}}{\mathrm{d}t} = R_h(\bar{Q}) \tag{22}$$

Then the third-order TVD Runge–Kutta scheme can be expressed as

$$\begin{aligned} \bar{Q}^{(1)} &= \bar{Q}^n + \Delta t\, R_h(\bar{Q}^n) \\ \bar{Q}^{(2)} &= \tfrac{3}{4}\bar{Q}^n + \tfrac{1}{4}\left[\bar{Q}^{(1)} + \Delta t\, R_h(\bar{Q}^{(1)})\right] \\ \bar{Q}^{n+1} &= \tfrac{1}{3}\bar{Q}^n + \tfrac{2}{3}\left[\bar{Q}^{(2)} + \Delta t\, R_h(\bar{Q}^{(2)})\right] \end{aligned} \tag{23}$$

Other aspects of the method such as data limiting, boundary conditions are included in Ref. 4. No special boundary conditions are implemented for the CAA problems presented in this paper. For example, the combined use of a buffer zone, grid coarsening, and a characteristic boundary condition serves as the far-field nonreflection boundary condition. A test case is designed to evaluate the effectiveness of such a boundary condition in the next section.

III. Numerical Tests

A. Propagation of a Density Pulse in an Abrupt Mesh

This test case is selected from the third Computational Aeroacoustics Workshop on Benchmark Problems[21] and was designed to evaluate the effects of mesh irregularity on aeroacoustic wave propagation. As mentioned in the preceding section, buffer layers with grid coarsening are used to serve as the nonreflection boundary condition at the far-field open boundaries in the present study. The justification behind this technique is to damp the outgoing waves through the use of grid coarsening such that wave reflections from

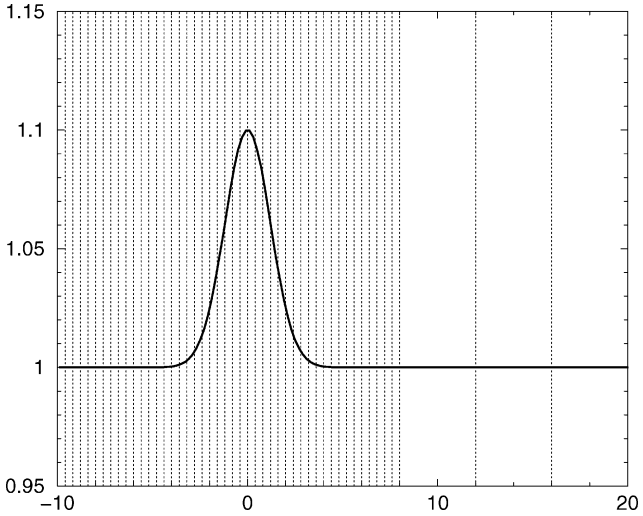

Fig. 2 Propagation of a density pulse in an abrupt grid, $\Delta x_2/\Delta x_1 = 10$.

the boundary, if any, are minimized. If there are reflected waves from the far-field boundary, these waves will again be damped as a result of the large artificial dissipations on the coarser mesh. The effectiveness of this technique hinges on minimum wave reflections by a nonuniform mesh. To test whether a nonuniform mesh produces large wave reflections, a mesh with a very abrupt change in spacing is used, that is, the mesh size changes by an order of magnitude from one region ($x < 8$) to a neighboring region ($x > 8$) as shown in Fig. 2. An initial density pulse in the form of a Gaussian is located at $x = 0$ and can be expressed as

$$\rho = 1 + 0.1\, e^{-\ln 2(x^2/2)}$$

The pressure and velocity are initialized to be 1, and the ratio of specific heats is set to be 1.4. Therefore the flow is subsonic, and the density pulse should propagate in the positive x direction with unit speed. Spectral volume schemes of various orders of accuracy are evaluated with this case. All of the schemes have the same number of DOFs, and the average mesh size per DOF for all schemes is 0.2 in the region $x < 8$ and 2 in the region $x > 8$. Therefore there is a very abrupt change in mesh size with a ratio of 10. Both fluxes formulas were tested. The computed waves at different times are displayed in Figs. 3–5 using the second-, fourth-, and sixth-order SV schemes, with both the Rusanov and Roe fluxes. First, it is obvious that the waves are damped heavily by all of the SV schemes when they cross $x = 8$ as a result of the inherent

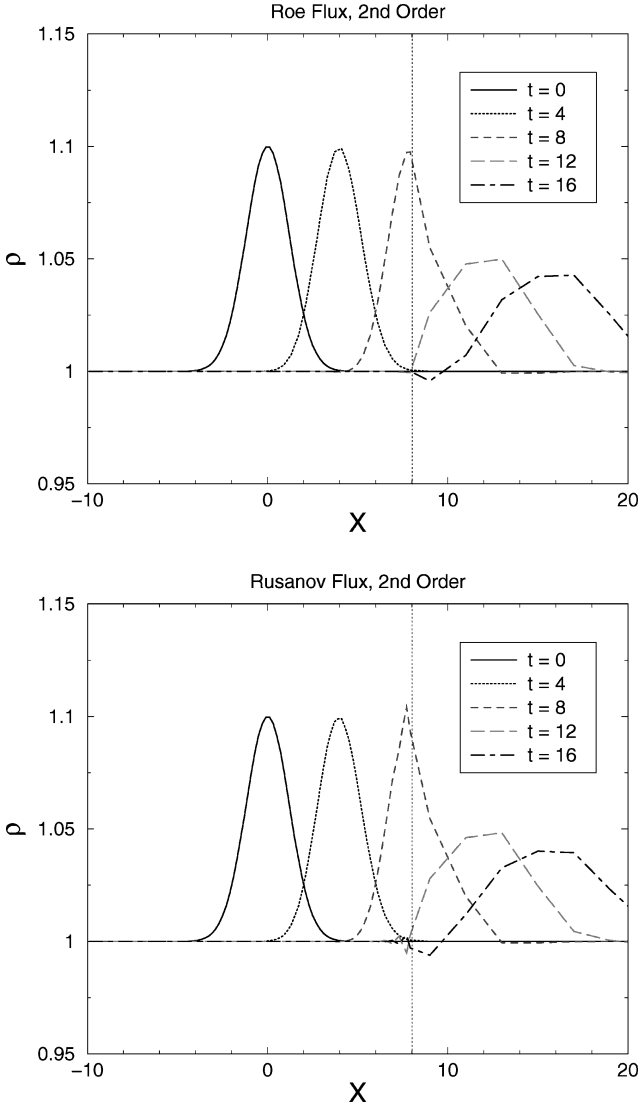

Fig. 3 Computed density wave at different times with the second-order SV scheme.

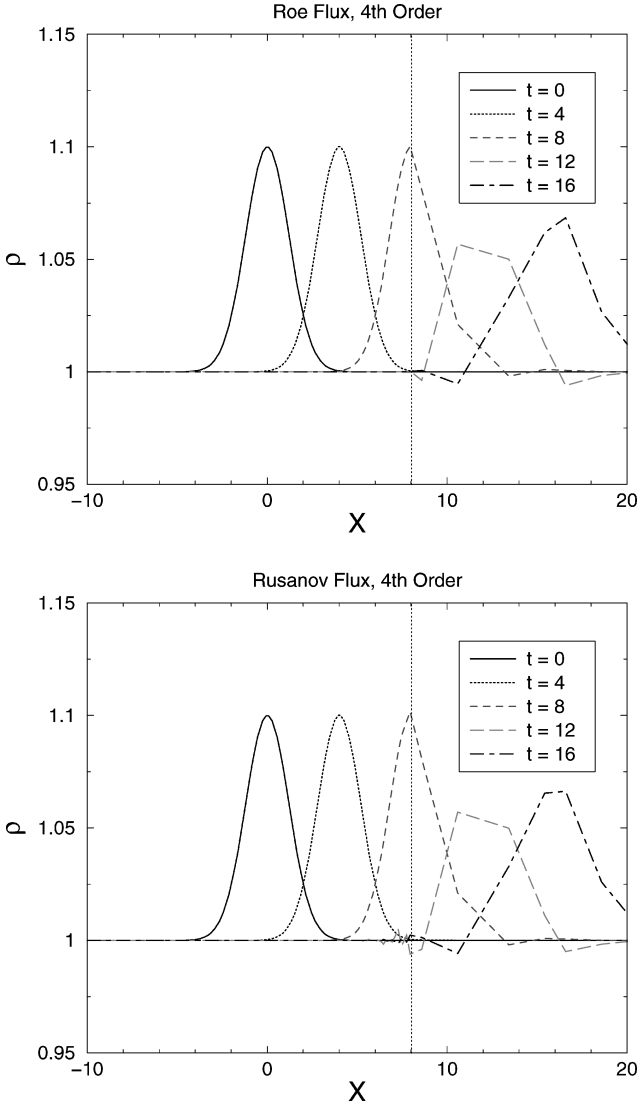

Fig. 4 Computed density wave at different times with the fourth-order SV scheme.

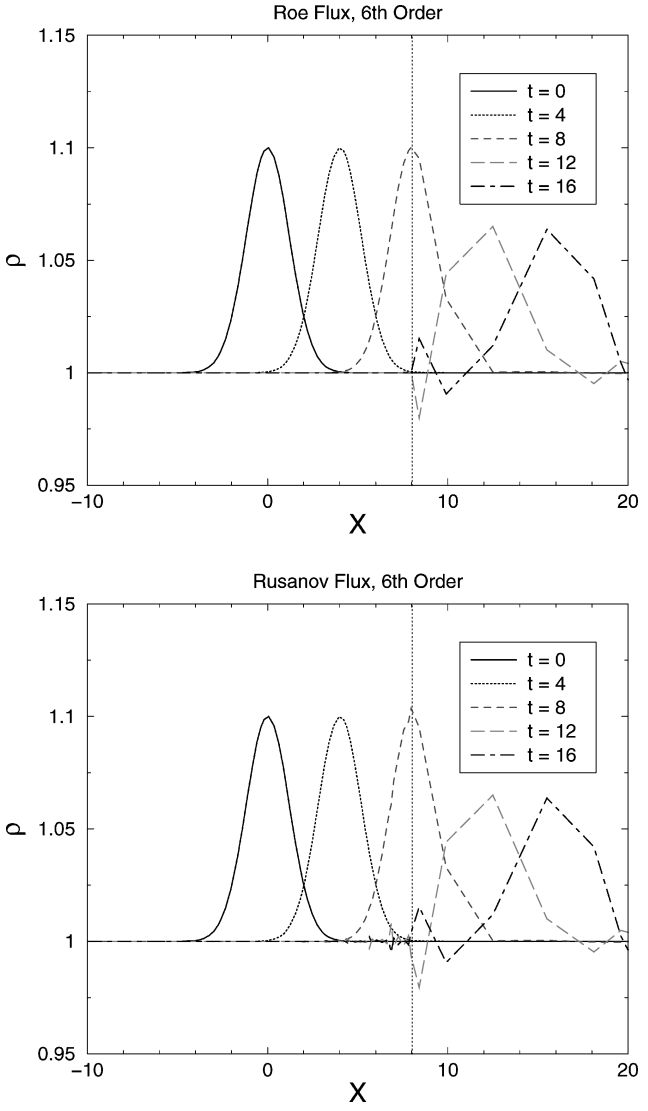

Fig. 5 Computed density wave at different times with the sixth-order SV scheme.

numerical dissipation, with the second-order SV scheme showing the most numerical damping. Second, the pulse becomes oscillatory after it crosses $x = 8$ for all of the numerical schemes because the wave is not properly resolved in all cases. Third, the oscillatory wave in the region of $x > 8$ propagates upstream with the Rusanov flux, but not with the Roe flux for all schemes. This is to say that the abrupt mesh causes negligible wave reflections with the Roe flux and significant reflections with the Rusanov flux as shown in Figs. 3–5. This phenomenon indicates that the Roe flux is preferred when severely nonuniform meshes are employed. The dramatic different performance of the Roe and Rusanov fluxes can be attributed to the more faithful handling of wave propagations by the Roe flux.

In the second test, a gradually coarsened grid with an expansion ratio of 2 is used, as shown in Fig. 6. The same simulations were repeated on this mesh using second-, fourth-, and sixth-order SV schemes and both the Roe and Rusanov fluxes. The computational results are displayed in Figs. 7–9. It is obvious that the magnitudes of the wave oscillations in the buffer zone are smaller on this grid than those on the previous grid using any of the SV schemes with either flux formula. Once again, the wave reflection from the mesh coarsening computed with the Roe flux is much smaller than that with the Rusanov flux. We also report that when the mesh expansion ratio is 1.2 all computations show negligible wave reflections. Roe's approximate solver will be used in all the rest of the computations.

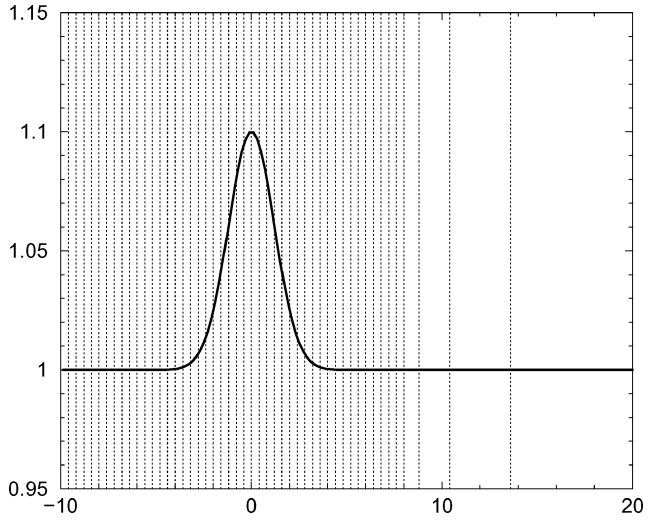

Fig. 6 Propagation of a density pulse in an abrupt grid, $\Delta x_2/\Delta x_1 = 2$.

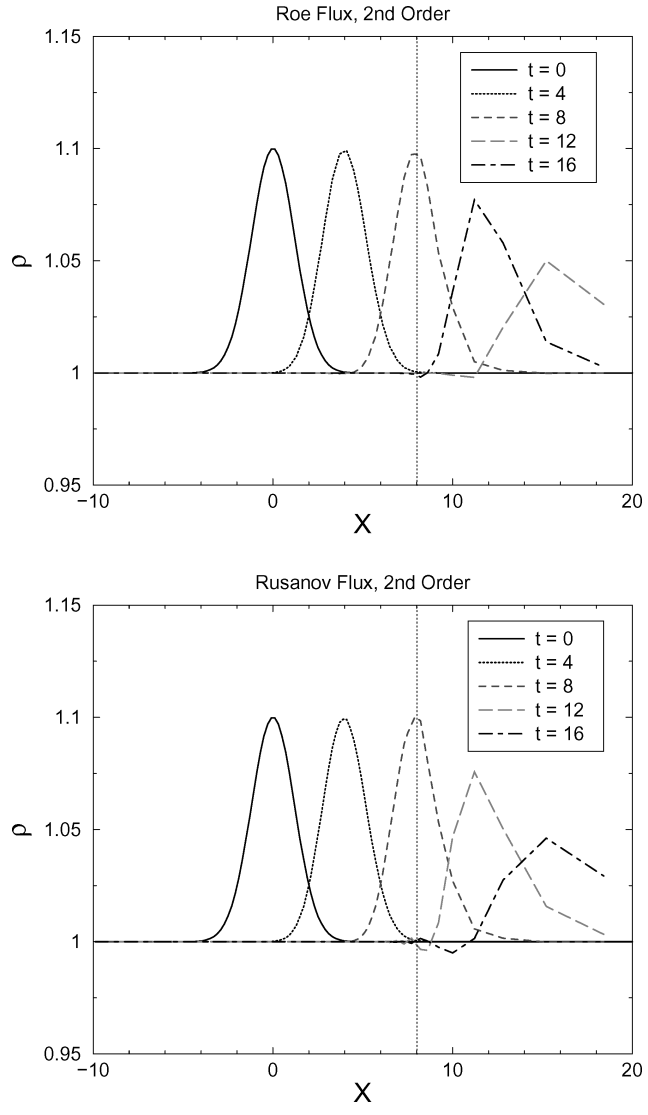

Fig. 7 Computed density wave at different times with the second-order SV scheme ($\Delta x_2/\Delta x_1 = 2$).

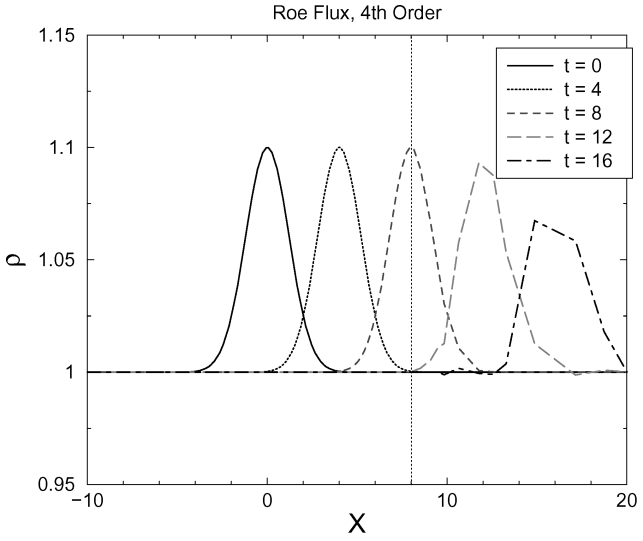

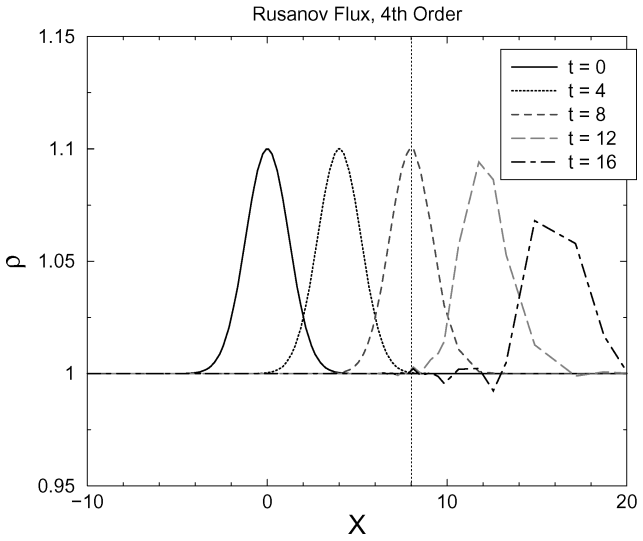

Fig. 8 Computed density wave at different times with the fourth-order SV scheme ($\Delta x_2/\Delta x_1 = 2$).

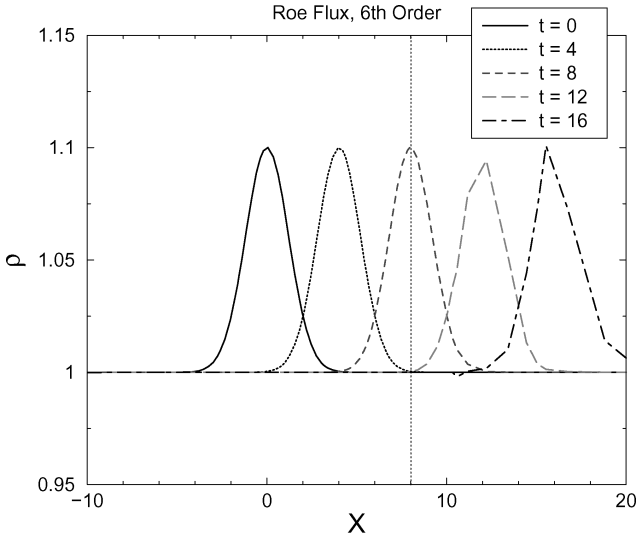

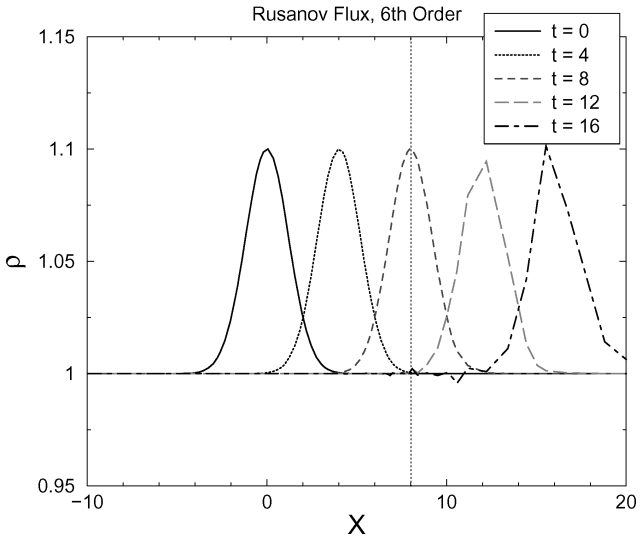

Fig. 9 Computed density wave at different times with the sixth-order SV scheme ($\Delta x_2/\Delta x_1 = 2$).

B. Sound Waves Through a Transonic Nozzle

This case is again selected from the Third Computational Aeroacoustics Workshop on Benchmark Problems.[21] A one-dimensional nozzle with the following area distribution is considered:

$$A(x) = \begin{cases} 0.536572 - 0.198086e^{-\ell_n 2(x/0.6)^2}, & x > 0 \\ 1.0 - 0.661514e^{-\ell_n 2(x/0.6)^2}, & x < 0 \end{cases}$$

The computational domain is $[-10, 10]$. The mean flow is completely subsonic with an exit Mach number of 0.4. Small-amplitude acoustics waves, with angular frequency $\omega = 0.6\pi$, are generated way downstream and propagate upstream through the narrow passage of the nozzle throat. The acoustic wave in the uniform region downstream of the nozzle can be represented by

$$\begin{bmatrix} \rho' \\ u' \\ p' \end{bmatrix} = \varepsilon \begin{bmatrix} 1 \\ -1 \\ 1 \end{bmatrix} \cos\left[\varpi\left(\frac{x}{1-M} + t\right)\right]$$

where $\varepsilon = 1.e{-}5$. Because nonlinear Euler equations were employed in the simulation, we need to first compute the mean flow solution.

In the initial test, only uniform grids were employed in order to remove the effects of the grid from the consideration. Three SV schemes with third-, fourth-, and sixth-order of accuracy were investigated with the same DOFs. Therefore, 200, 150, and 100 SVs were used for the third-, fourth-, and sixth-order schemes, respectively, resulting in a total of 600 DOFs. Characteristic boundary conditions were used in both the inlet and exits based on the propagating directions of the waves. The mean flow solutions from all three schemes are plotted in Fig. 10. Note that the solutions agree very well with each other, indicating that the mean flow solution is scheme and grid independent. The mean flow solution was then used as the initial condition for the unsteady simulation. The

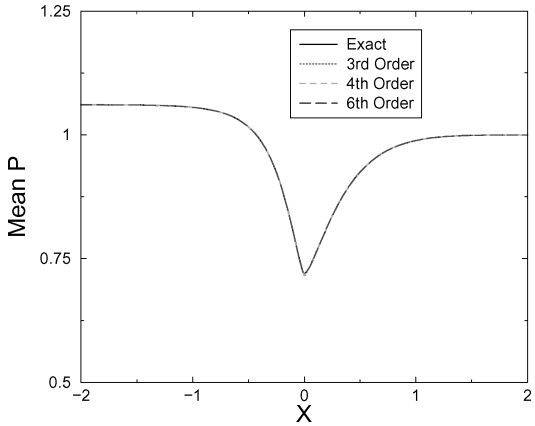

Fig. 10 Computed and analytical mean pressures for the subsonic flow through a converging-diverging nozzle.

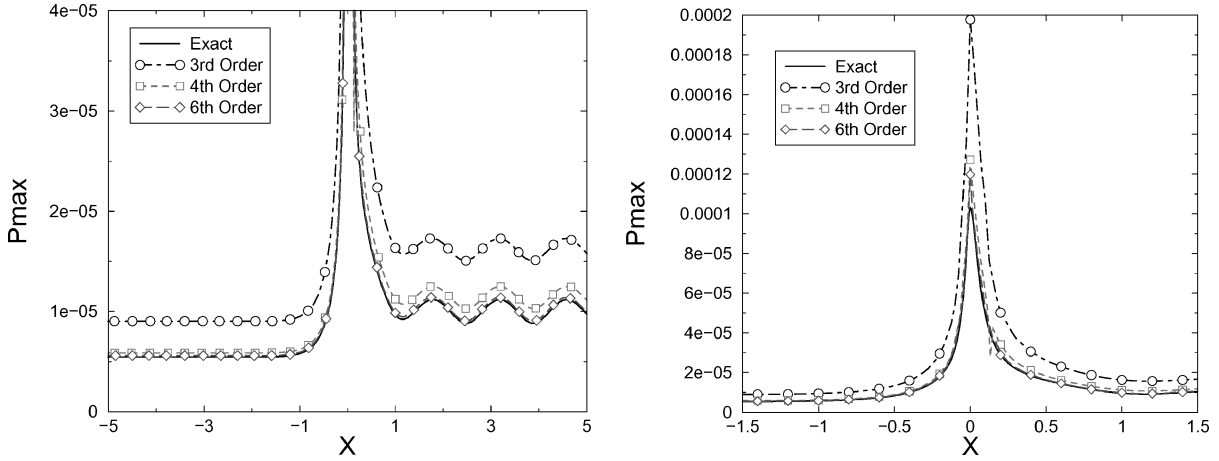

Fig. 11 Comparison of computed and exact maximum acoustic pressures.

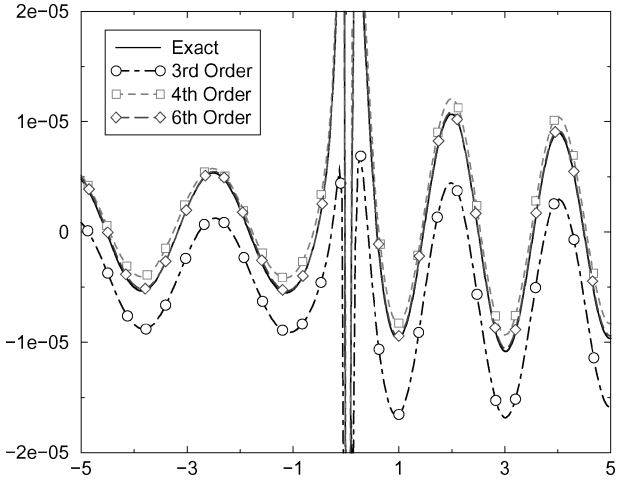

Fig. 12 Comparison of computed and exact instantaneous acoustic pressures.

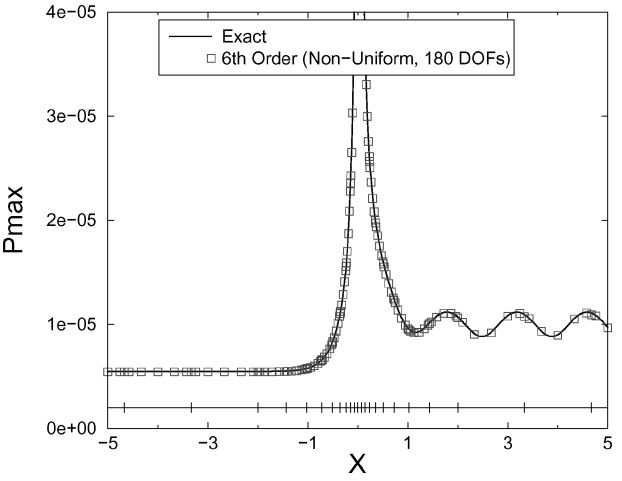

Fig. 13 Computed maximum acoustic pressure on the nonuniform grid, with comparison to the exact solution.

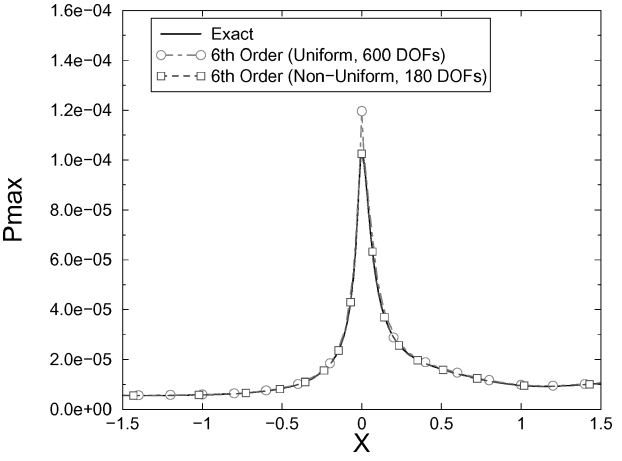

Fig. 14 Computed maximum acoustic pressures on both the uniform and nonuniform grids.

unsteady upstream-propagating acoustic waves are imposed directly on the right side of the downstream boundary face, with the left-side state variables reconstructed from the interior domain. The Riemann solver automatically takes care of the wave propagation. The unsteady solution becomes periodic after $t = 40$. The maximum acoustic pressure is then determined over several periods. The maximum acoustic pressures computed with the SV schemes are compared with the analytical solution in Fig. 11. As expected, the sixth-order scheme produces much more accurate results than the third- and fourth-order schemes with the same DOFs. In terms of the computational cost for this case, the third-, fourth-, and sixth-order schemes are very similar because the total number of flux evaluations is the same. Although the sixth-order scheme takes more CPU time in the reconstruction, it requires less Riemann flux evaluations than the fourth- or third-order schemes. The computed instantaneous acoustic pressure distributions are compared with the analytical solution in Fig. 12. Again, the sixth-order SV scheme performs the best.

Because the acoustic waves have much higher frequencies near the throat than those in the constant-area downstream region, a better computational mesh can be produced by clustering the grid points near the throat. Such a mesh with 30 SVs was generated, and the maximum SV is about 20 times larger than the minimum SV. The sixth-order SV scheme was then employed on this nonuniform mesh to carry out the same simulation with 180 DOFs. The computed maximum acoustic pressure is compared with the analytical solution in Fig. 13, which also displays the computational mesh. For comparison purposes, the computed maximum acoustic pressures on both the uniform and nonuniform grids are compared with the analytical solution in Fig. 14. With only 180 DOFs, the computed acoustic pressure on the nonuniform grid agrees better than that on the uniform grid with 600 DOFs. Finally the computed instantaneous pressure is plotted with the analytical solution in Fig. 15. They are right on top of each other.

C. Shock-Sound Interaction

This case is again selected from the Third Computational Aeroacoustics Workshop on Benchmark Problems. The nozzle geometry is the same as in the preceding case. The mean flow is supersonic

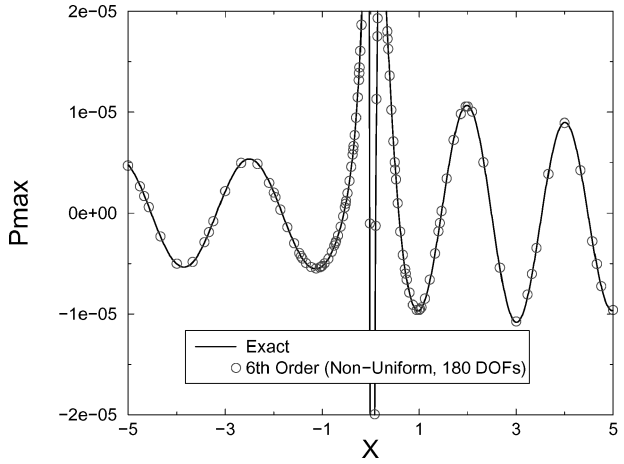

Fig. 15 Comparison of computed and exact instantaneous acoustic pressures.

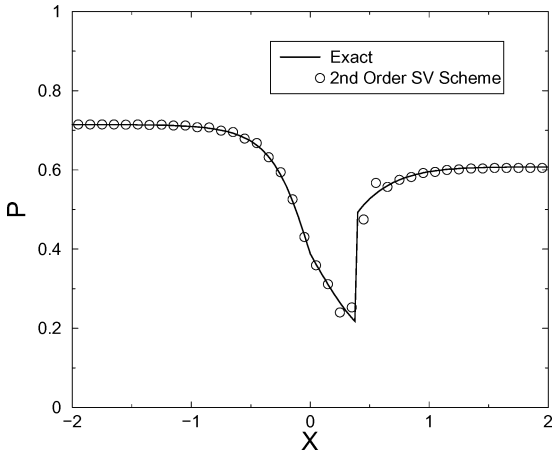

Fig. 16 Computed and analytical mean pressures for the supersonic flow through a Laval nozzle.

at the inlet, and the exit pressure is so designed that a shock wave is generated downstream of the throat. At the inflow boundary, the conditions are

$$\begin{bmatrix}\rho\\ u\\ p\end{bmatrix} = \begin{bmatrix}1\\ M\\ 1/\gamma\end{bmatrix} + \varepsilon \begin{bmatrix}1\\ 1\\ 1\end{bmatrix} \sin\left[\varpi\left(\frac{x}{1+M} - t\right)\right]$$

where $e = 1.e{-}5$, $\omega = 0.6\pi$, and $M_{\text{inlet}} = 0.2006533$. The exit pressure is set to be 0.6071752 to create a shock. A uniform grid with 100 SVs and the second-order SV scheme were used in the simulation. Although higher-order SV schemes were tried, it appeared that the limiters had a detrimental effect on the acoustic waves. Designing acoustic-wave preserving limiters will be a future research topic. The computed mean pressure is compared with the analytical solution in Fig. 16. The agreement is good, though the numerical solution is slightly oscillatory. It would be interesting to see whether this small oscillation affects the acoustic waves. The computed instantaneous acoustic pressure is displayed with the analytical solution in Fig. 17. It seems the small oscillation does not seriously affect the acoustic waves, and the acoustic waves are free to propagate across the shock wave. The pressure history at the exit is plotted in Fig. 18 with the analytical solution. Generally speaking, the agreement is very good.

D. Scattering of Acoustic Pulse from a Cylinder

This case is a benchmark problem denoted as category I, problem 2, in the second CAA Workshop. The configuration describes the scattering off a circular cylinder of a prescribed initial pressure

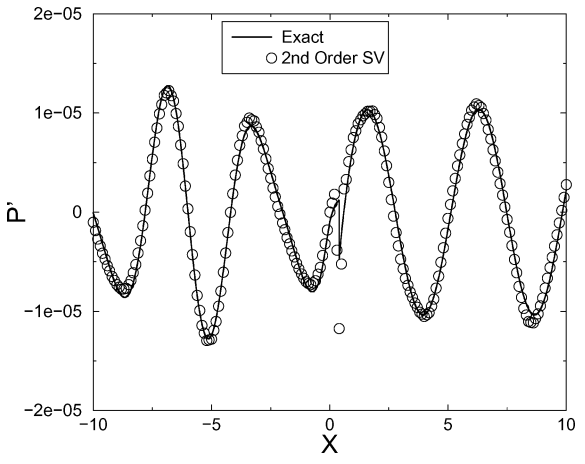

Fig. 17 Comparison of computed and exact instantaneous acoustic pressures.

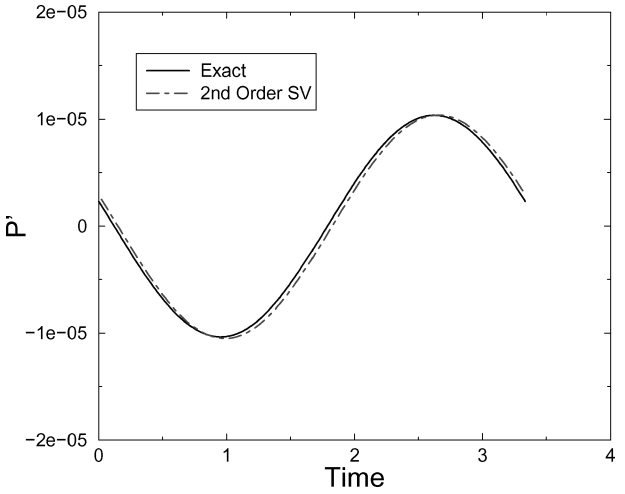

Fig. 18 Comparison of pressure histories at the nozzle exit.

pulse. The pulse is given by

$$p = p_\infty \left\{1 + \varepsilon \exp\left[-\ell_n 2 \frac{(x-x_c)^2 + (y-y_c)^2}{b^2}\right]\right\}$$

In the present simulation, the following parameters are chosen: $x_c = 4$, $y_c = 0$, $\varepsilon = 0.01$, and $b = 0.2$. The mean flow conditions are $\rho_\infty = 1$ and $p_\infty = 1/1.4$. Because of symmetry, only the top half is selected as the computational domain. The computational mesh has two zones. The inner zone is within the half-circle of $r = 7$, whereas the outer zone extends between $r = 7$ and 9 with a constant mesh size expansion factor of 1.1. The outer zone serves as the buffer zone, which is used to reduce the reflected waves from the outer boundary. Several computational grids with mesh sizes of 0.07 (finest), 0.1 (fine), 0.15 (medium), 0.2 (coarse), and 0.25 (coarsest) were generated and employed in the simulation. They have 37,859; 18,478; 8783; 5432; and 3794 triangles (SVs), respectively, in the inner zone. The medium computational mesh is shown in Fig. 19. All of the simulations were carried out until $t = 10$ with a time step between 0.002 and 0.004. The computed pressure fields with the fourth-order SV scheme on the medium mesh at four different times are shown in Fig. 20. Because each triangle (SV) is further partitioned into 10 subcells (CVs) using the fourth-order SV scheme, this simulation has a total of 87,830 DOFs. It appears that the outgoing waves were heavily damped in the buffer zone and able to exit the outer boundary without visible reflections. Computations were also performed on the two coarser meshes using the fourth-order SV scheme to study grid convergence. The computational histories of acoustic pressure at two selected locations (0, 5) and (−5, 0) on the three coarsest meshes are compared with the analytical solution

in Fig. 21. Note that the finer the computational grid, the better the agreement with the analytical solution. It is evident that even the coarsest mesh produced acceptable computational results with the fourth-order SV scheme.

Next the lower-order SV schemes were evaluated by performing the same simulations to compare the relative accuracy of the schemes and demonstrate the advantages of the higher-order scheme. For this purpose, the second-order SV scheme was employed on the finest mesh, and the third-order SV scheme was used on the fine mesh to carry out the simulation. Therefore the second-order simulation has $37{,}859 \times 3 = 113{,}577$ DOFs, whereas the third-order simulation has $18{,}468 \times 6 = 110{,}868$ DOFs. The computational histories of acoustic pressure at the same two locations are compared with the analytical solution in Fig. 22. The results computed with the fourth-order SV scheme on the coarse mesh are much better than those computed with the second- and third-order SV schemes on the much finer grids. Both the lower-order schemes showed larger errors in the pressure history. For these computations, the third- and fourth-order SV schemes took 2.57 and 1.67 times of the CPU time of the second-order SV scheme, respectively. The fourth-order SV scheme not only produced more accurate results, but also took less CPU time than the third-order SV scheme.

E. Two-Cylinder-Wave Diffraction Problem

This case is a benchmark problem denoted as category II, problem 1, in the fourth CAA Workshop on Benchmark Problems. The scattering of a periodic acoustic source from two circular cylinders

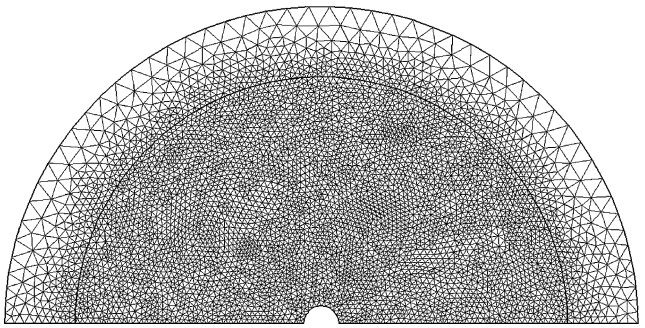

Fig. 19 Fully unstructured triangular grid with mesh size of 0.15 (medium grid).

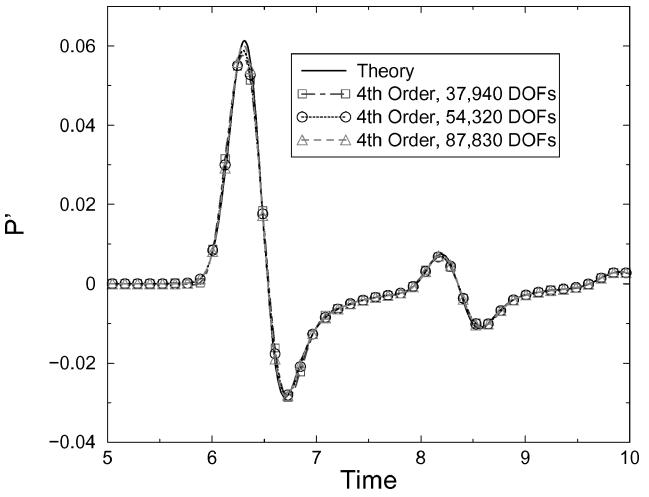

a) At (0, 5)

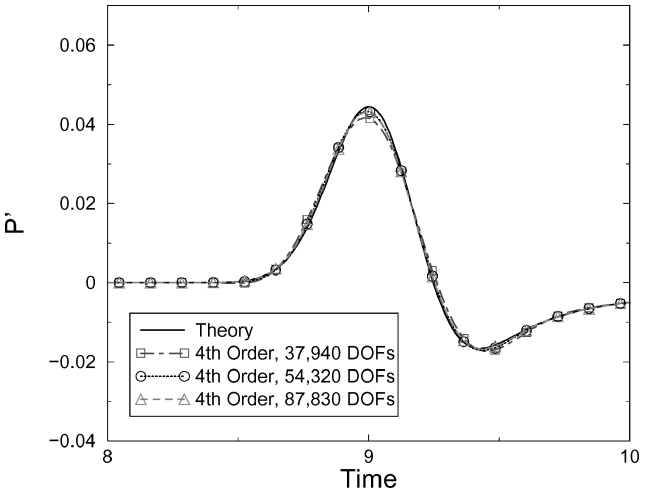

b) At (−5, 0)

Fig. 21 Comparison of pressure histories computed with the fourth-order SV scheme on different grids.

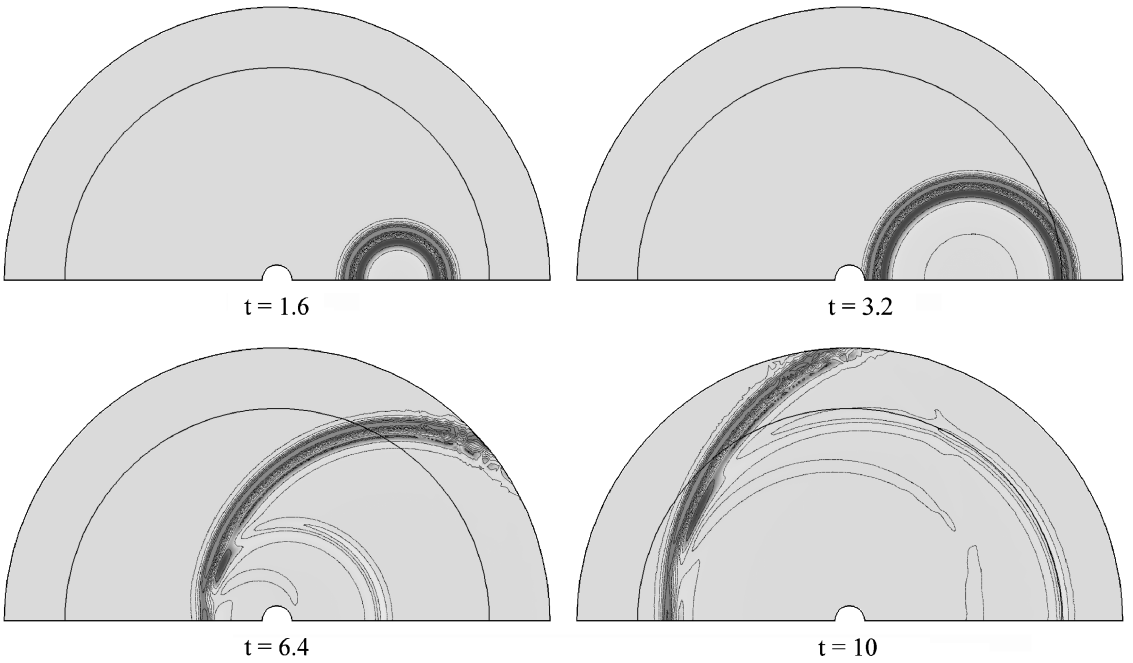

Fig. 20 Pressure contours at various instants computed with the fourth-order SV scheme on the medium grid.

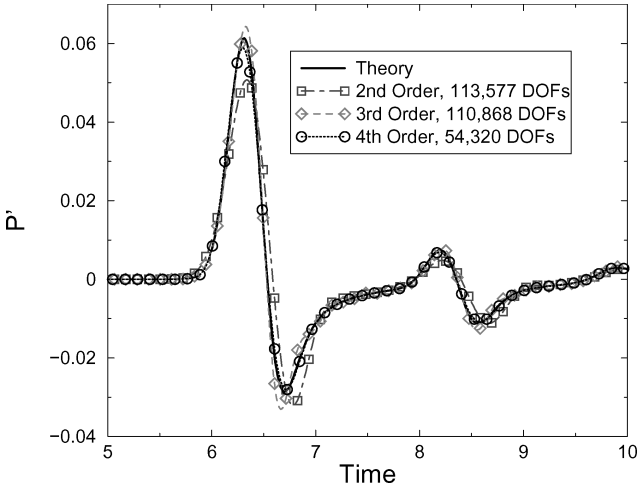

a) At (0, 5)

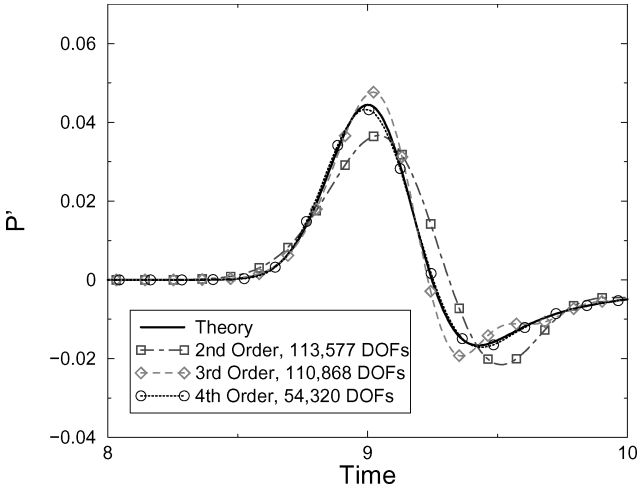

b) At (0, −5)

Fig. 22 Comparison of pressure histories computed with different SV schemes.

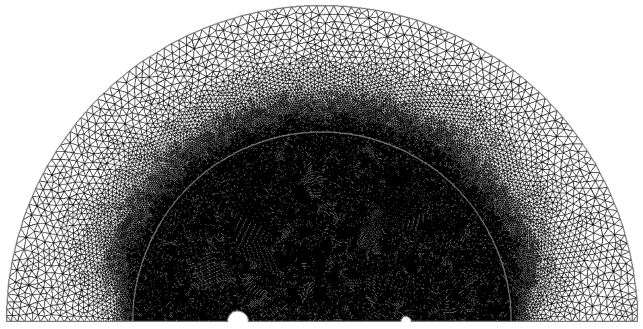

Fig. 23 Computational grid for the two-cylinder diffraction problem.

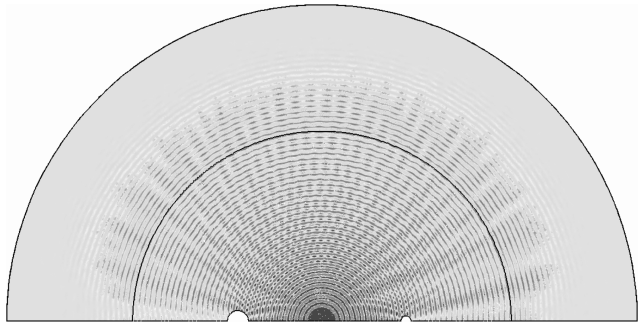

Fig. 24 Pressure distribution computed with the fourth-order SV scheme.

is considered. The acoustic source used in this case has a transient term expressed in the following form[17]:

$$S = e^{-\ell_n 2[(x^2+y^2)/0.2^2]} \sin(\omega t) f(t), \qquad f(t) = \min\left[1, (t/t_0)^3\right]$$

The following parameters are chosen in the present study: $\varpi = 8\pi$ and $t_0 = 4$. Because the configuration is symmetric, only the upper half of the physical domain is used in the computation. The computational mesh is displayed in Fig. 23. The entire computational domain extends to $r = 15$. The grid within $r = 9$ is nearly uniform with a mesh size = 0.06. Because each triangle is further partitioned

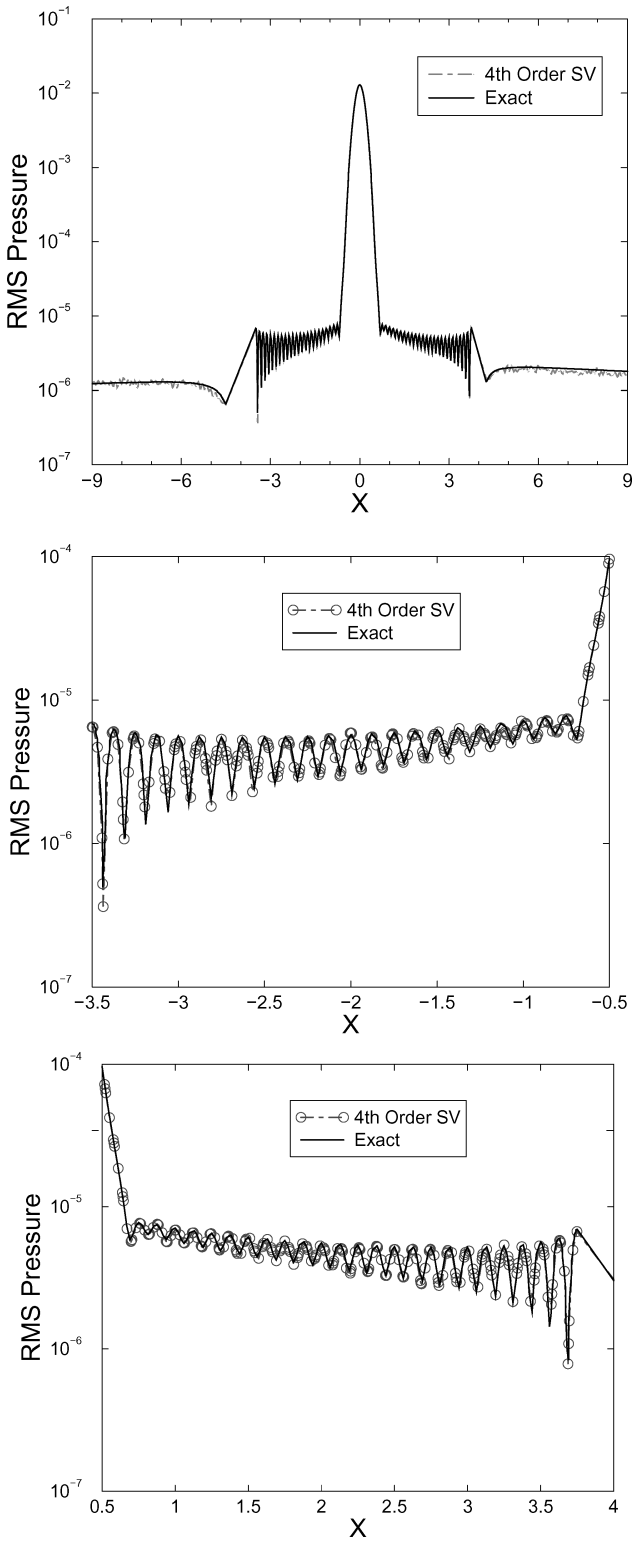

Fig. 25 Comparison of the computational and analytical rms pressure along the center line.

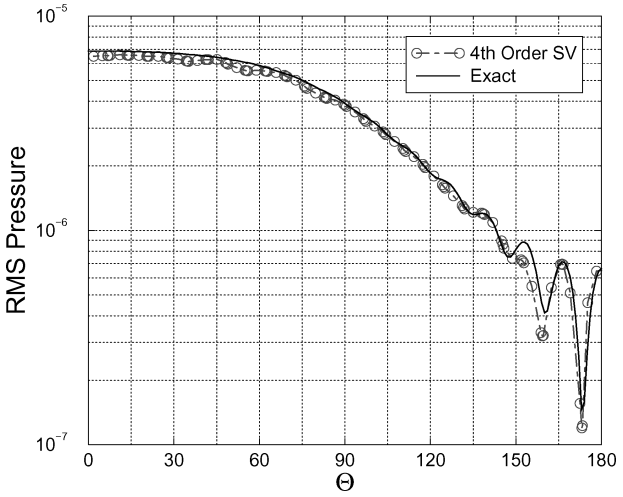

a) Left cylinder

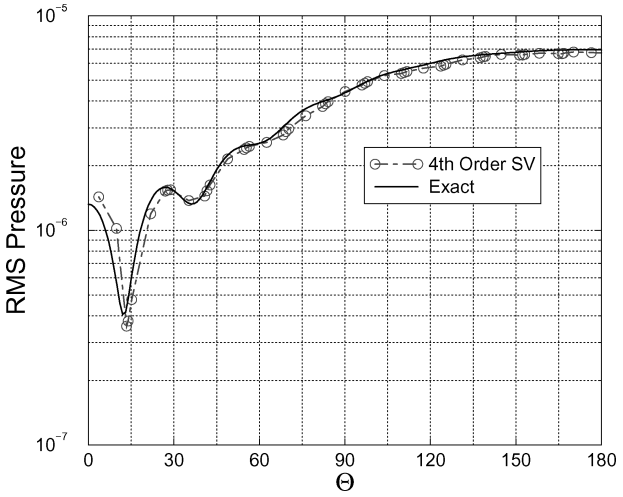

b) Right cylinder

Fig. 26 Comparison of the computational and analytical rms pressure along the two cylinders.

into 10 subcells, the grid has an equivalent points per wave of about 13 [sqrt(10)*0.25/0.06]. The mesh is coarsened from $r = 9$ to 15 with an expansion factor of 1.1 to serve as the buffer zone. A constant time step of 0.002 was used in the computation with a total of 20,000 time steps. The fourth-order SV scheme was employed in the computation. The rms pressure is computed in the last 2000 time steps. The computed pressure field at a certain time is shown in Fig. 24. Note that the outgoing waves are significantly damped in the buffer zone without visible reflections. The computed rms pressure along the centerline is compared with the analytical solution[22] in Fig. 25. The rms pressure on the two cylinder surfaces is also compared with the analytical solution in Fig. 26. Note that the agreement between the computation and analytical solutions is good with the current grid resolution.

F. Three-Cylinder-Wave Diffraction Problem

This case is a benchmark problem denoted as category II, problem 2, in the fourth CAA Workshop on Benchmark Problems. The scattering of a periodic acoustic source from three circular cylinders is considered. Because of flow symmetry, only the top half of the physical domain is used in the computation. The computational mesh is displayed in Fig. 27. Again the mesh has an inner zone inside $r = 9$ and an outer buffer zone from $r = 9$ to 14. The inner zone has a grid size of 0.06. The mesh is coarsened from $r = 9$ to 14 with an expansion factor of 1.1 to serve as the buffer zone. A constant time step of 0.002 was used in the computation with a total of 20,000 time steps. The fourth-order SV scheme was employed in the computation. The rms pressure is computed in the last 2000

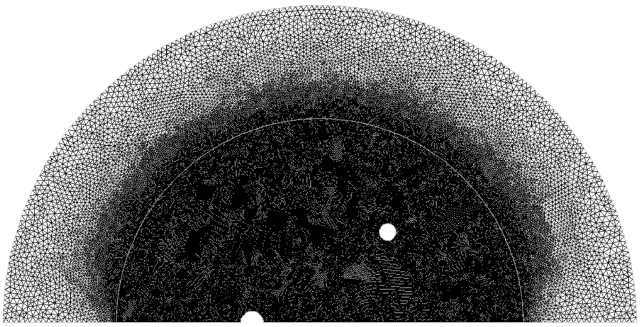

Fig. 27 Computational grid for the three-cylinder diffraction problem.

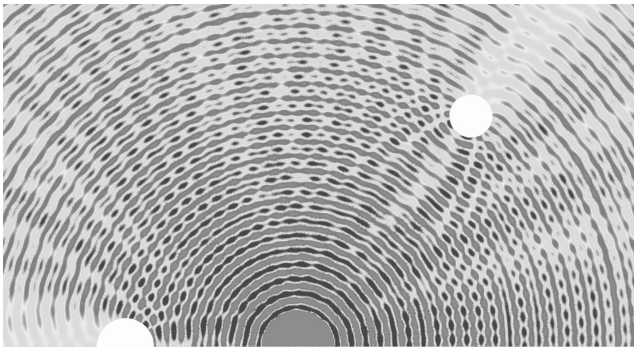

Fig. 28 Pressure distribution computed with the fourth-order SV scheme.

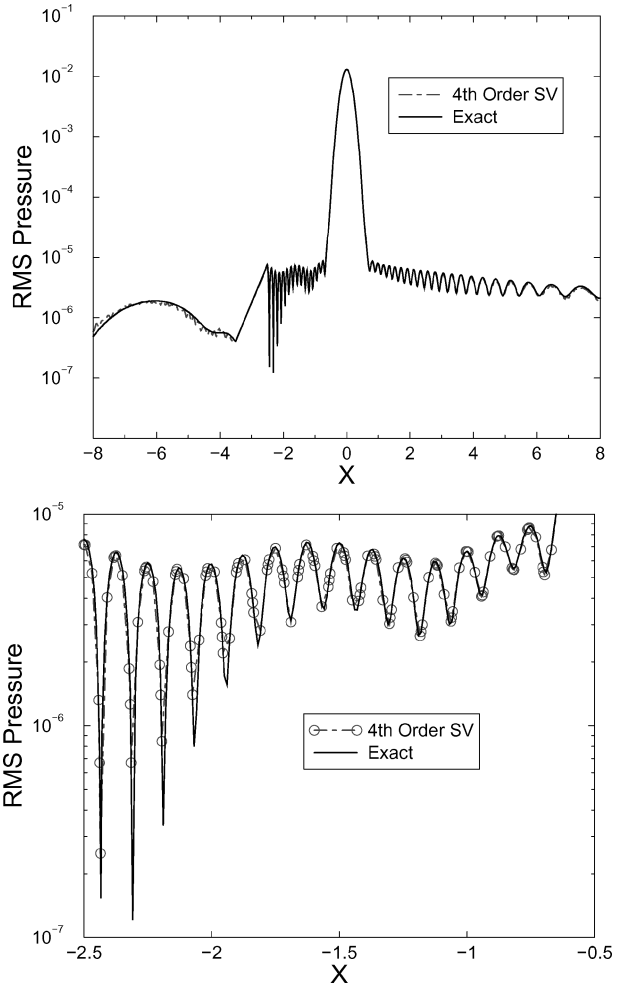

Fig. 29 Comparison of the computational and analytical rms pressure along the center line.

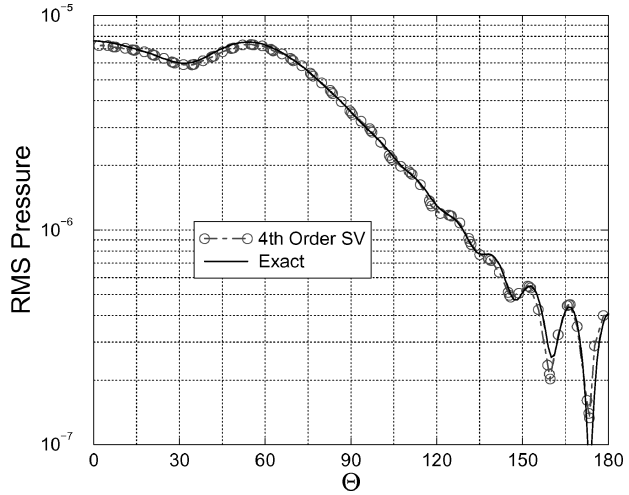

a) Left cylinder

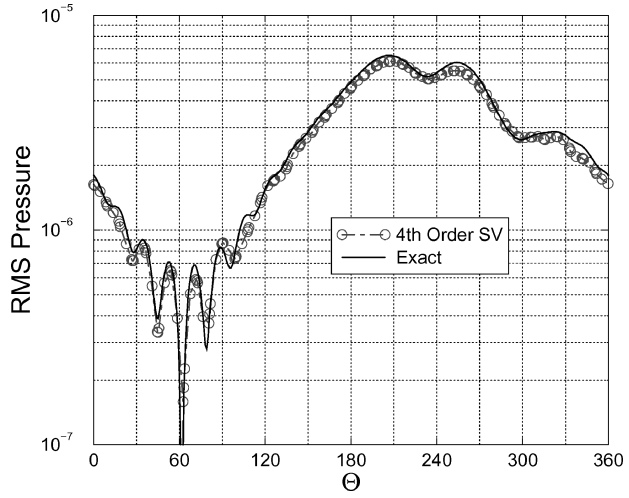

b) Right cylinder

Fig. 30 Comparison of the computational and analytical rms pressure along the two cylinders.

time steps. The computed pressure field is shown in Fig. 28. The computed rms pressure along the centerline is compared with the analytical solution in Fig. 29. The rms pressure on the two cylinder surfaces is also compared with the analytical solution in Fig. 30. Note that there is good agreement between the computation and analytical solutions.

IV. Conclusions

The spectral volume (SV) method has been tested on several benchmark computational aeroacoustics (CAA) problems in this paper. It is clearly demonstrated that high-order schemes are required to deliver the expected solution accuracy in CAA problems, and they do perform much better than lower-order ones. For the wave scattering problems, the fourth SV scheme was capable of producing reasonable results with a grid resolution of about 13 points per wave. The advantage of the SV method over high-order methods on structured grids lies in its capability of handling complex geometries in a very flexible manner. The problems can all be set up in minutes. It is also found that limiters have a detrimental effect on the acoustic waves. Acoustic-wave preserving limiters are necessary for the high-order schemes to handle shock-sound-wave interactions efficiently, and this will be a future research topic.

Acknowledgments

The author gratefully acknowledges the Intramural Research Grant Project awarded by Michigan State University and the startup funding provided by the Department of Mechanical Engineering, College of Engineering of Michigan State University. Some of the work presented in the paper was conducted while the author was visiting the U.S. Air Force Research Laboratory (AFRL), Dayton, Ohio, with support from the AFRL's summer faculty program. The author thanks Miguel Visbal and Scott Sherer for many helpful discussions and for providing the analytical solutions for the category 2 problems from the fourth CAA Workshop.

References

[1]Wang, Z. J., "Spectral (Finite) Volume Method for Conservation Laws on Unstructured Grids: Basic Formulation," *Journal of Computational Physics*, Vol. 178, No. 1, 2002, pp. 210–251.

[2]Wang, Z. J., and Liu, Y., "Spectral (Finite) Volume Method for Conservation Laws on Unstructured Grids II: Extension to Two-Dimensional Scalar Equation," *Journal of Computational Physics*, Vol. 179, No. 2, 2002, pp. 665–697.

[3]Wang, Z. J., and Liu, Y., "Spectral (Finite) Volume Method for Conservation Laws on Unstructured Grids III: Extension to One-Dimensional Systems," *Journal of Scientific Computing*, Vol. 20, No. 1, 2004, pp. 137–157.

[4]Wang, Z. J., Zhang, L., and Liu, Y., "Spectral (Finite) Volume Method for Conservation Laws on Unstructured Grids IV: Extension to Two-Dimensional Euler Equations," *Journal of Computational Physics*, Vol. 194, No. 2, 2004, pp. 716–741.

[5]Godunov, S. K., "A Finite-Difference Method for the Numerical Computation of Discontinuous Solutions of the Equations of Fluid Dynamics," *Matematicheskii Sbornik*, Vol. 47, 1959, p. 271.

[6]Van Leer, B., "Towards the Ultimate Conservative Difference Scheme V. A Second Order Sequel to Godunov's Method," *Journal of Computational Physics*, Vol. 32, No. 1, 1979, pp. 101–136.

[7]Cockburn, B., Hou, S., and Shu, C.-W., "TVB Runge–Kutta Local Projection Discontinuous Galerkin Finite Element Method for Conservation Laws IV: The Multidimensional Case," *Mathematics of Computation*, Vol. 54, 1990, pp. 545–581.

[8]Bassi, F., and Rebay, S., "High-Order Accurate Discontinuous Finite Element Solution of the 2D Euler Equations," *Journal of Computational Physics*, Vol. 138, No. 2, 1997, pp. 251–285.

[9]Kopriva, D. A., and Kolias, J. H., "A Conservative Staggered-Grid Chebyshev Multidomain Method for Compressible Flows," *Journal of Computational Physics*, Vol. 125, No. 1, 1996, pp. 244–261.

[10]Abarbanel, S., Gottlieb, D., and Hesthaven, J. S., "Wellposed Perfectly Matched Layers for Advective Acoustics," *Journal of Computational Physics*, Vol. 154, No. 2, 1999, pp. 266–283.

[11]Sun, Y., and Wang, Z. J., "Evaluation of Discontinuous Galerkin and Spectral Volume Methods for Scalar and System Conservation Laws on Unstructured Grids," *International Journal for Numerical Methods in Fluids*, Vol. 45, No. 8, 2004, pp. 819–838.

[12]Zhang, M., and Shu, C.-W., "An Analysis of and a Comparison Between the Discontinuous Galerkin and Spectral Finite Volume Method," *Computers and Fluids* (to be published).

[13]Barth, T. J., and Frederickson, P. O., "High-Order Solution of the Euler Equations on Unstructured Grids Using Quadratic Reconstruction," AIAA Paper 90-0013, Jan. 1990.

[14]Tam, C. K. W., "Computational Aeroacoustics: Issues and Methods," *AIAA Journal*, Vol. 33, No. 10, 1995, pp. 1788–1796.

[15]Lele, S. K., "Compact Finite Difference Schemes with Spectral-Like Resolution," *Journal of Computational Physics*, Vol. 103, No. 1, 1992, pp. 16–42.

[16]Tam, C. K. W., and Webb, J. C., "Dispersion-Relation-Preserving Finite Difference Schemes for Computational Acoustics," *Journal of Computational Physics*, Vol. 107, No. 2, 1993, pp. 262–281.

[17]Visbal, M., and Gaitonde, D. V., "Computation of Aeroacoustic Fields on General Geometries Using Compact Differencing and Filtering Schemes," AIAA Paper 99-3706, June 1999.

[18]Rusanov, V. V., "Calculation of Interaction of Non-Steady Shock Waves with Obstacles," *Journal of Computational Mathematics and Physics, USSR*, Vol. 1, 1961, pp. 267–279.

[19]Roe, P. L., "Approximate Riemann Solvers, Parameter Vectors, and Difference Schemes," *Journal of Computational Physics*, Vol. 43, No. 2, 1981, pp. 357–372.

[20]Shu, C.-W., "Total-Variation-Diminishing Time Discretizations," *SIAM Journal on Scientific and Statistical Computing*, Vol. 9, 1988, pp. 1073–1084.

[21]Tam, C. K. W., Sankar, L. N., and Huff, D. L., "Third Computational Aeroacoustics (CAA) Workshop on Benchmark Problems," NASA CP-2000-209790, Nov. 1999.

[22]Sherer, S., and Visbal, M., "Computational Study of Acoustic Scattering from Multiple Bodies Using a High-Order Overset Grid Approach," AIAA Paper 2003-3203, July 2003.

D. Gaitonde
Associate Editor